JOURNAL OF FUEL CHEMISTRY AND TECHNOLOGY
Volume 54, Issue 8, August 2026

燃料化学学报(中英文)
Journal of Fuel Chemistry and Technology

Cite this article as: J Fuel Chem Technol, 2026, 54, 20250359

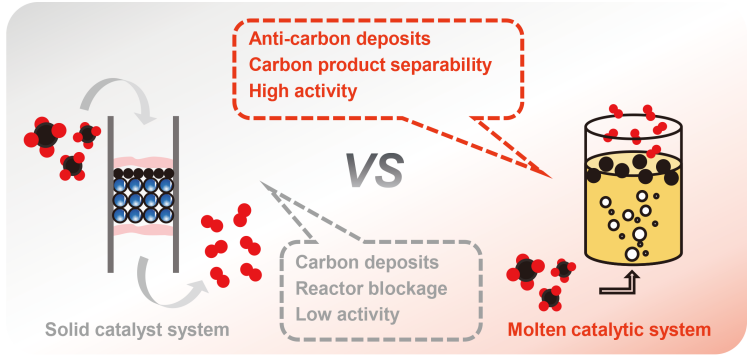
REVIEW

Research progress on hydrogen and carbon materials production from methane pyrolysis

ZHOU Luyuan[1], WANG Yang[1,*], SUN Yu[1], HUO Kaixuan[1], DONG Pei[2,*], WU Mingbo[1,3,*]

[1] College of Chemistry and Chemical Engineering, College of New Energy, China University of Petroleum (East China), Qingdao 266580, China;
[2] School of Environmental and Municipal Engineering, Qingdao University of Technology, Qingdao 266033, China;
[3] College of Chemical Engineering, Qingdao University of Science & Technology, Qingdao 266042, China

Abstract: The increase in social development and human activities has exacerbated challenges such as global warming and climate change, necessitating the exploration of efficient and clean alternative energy sources to mitigate global carbon emissions. Hydrogen energy is recognized as a crucial energy carrier for reducing carbon emissions due to its high combustion value (120 MJ/kg) and net-zero carbon emissions. Recently, the catalytic pyrolysis of methane for hydrogen production has garnered significant attention because it can simultaneously produce high-purity hydrogen and functional carbon materials. The primary challenges associated with this method include the development of catalysts that exhibit both high activity and resistance to deactivation caused by carbon deposition, as well as the efficient separation and high-value utilization of carbon products. Precise control of active sites, alloying strategies, support optimization, and tuning of the carbon-catalyst interface can significantly enhance the carbon-deposition resistance of solid catalysts. The introduction of catalytic systems based on molten media and the utilization of their dynamically refreshed gas-liquid reaction interfaces can fundamentally reduce deactivation and facilitate continuous carbon separation. This paper systematically reviews progress in solid and molten-medium catalysts for methane pyrolysis to produce hydrogen and carbon. It emphasizes reaction mechanisms, catalytic performance and mechanisms that control carbon morphology. The paper also discusses the strategies for efficient separation and purification of carbon products in molten media and explores the high-value application prospects of carbon products.



Key words: methane pyrolysis; hydrogen production; carbon materials; molten media

To meet the urgent global goal of limiting temperature increases to 1.5 °C annually, establishing a clean, low-carbon energy system has garnered extensive international support[1−2]. The reliance on traditional fossil fuels has greatly hindered the successful establishment of new energy system, as the combustion of fossil fuels is the major source of global greenhouse gas emissions. In this context, the energy transition centers on identifying zero-carbon energy carriers that can replace fossil fuels on a large scale. Hydrogen energy is highly valued for its substantial benefits. (1) It offers a high combustion calorific value, about three times that of gasoline. (2) It produces zero carbon emissions during use, serving as an effective energy storage medium. (3) It is adaptable to various applications. The international community regards hydrogen energy as a crucial solution for achieving deep decarbonization, particularly in “hard-to-decarbonize” sectors like industry, heavy transportation, and the chemical industry. It acts as a

Received: 2025-11-10; Revised: 2025-12-18
Foundation items: Supported by National Natural Science Foundation of China (22508211, 22478436).
* Corresponding author. Tel: 0532-86983801, E-mail: wangyang@upc.edu.cn, dongpei@upc.edu.cn, wumb@upc.edu.cn.
DOI: 10.1016/S1872-5813(26)60681-0 CSTR: 32157.14.2097-213X.2026.JFCT.0038
本文的英文电子版由 Elsevier 出版社在 ScienceDirect 上出版 (http://www.sciencedirect.com/science/journal/18725813)

bridge between intermittent renewable energy sources and a stable energy supply and serves as a strategic pillar for guiding energy, industrial, and transportation systems toward net-zero emissions[3]. Currently, global hydrogen production exceeds 75 million tons annually, yet energy system remains heavily dependent on fossil fuel sources[4].

The global hydrogen supply largely depends on fossil fuel reforming methods, which pose significant carbon and cost challenges. The steam methane reforming (SMR) process used to produce "gray hydrogen" is particularly carbon-intensive[5−6]. While the "blue hydrogen" pathway, including carbon capture and storage (CCS), can reduce carbon emissions to some extent, but it faces limitations such as maximum capture rates, dependence on geological storage and increased costs[7]. Water electrolysis provides an alternative pathway to produce "green hydrogen" with nearly zero carbon emissions throughout its lifecycle. However, its large-scale development is hampered by the high energy demands of hydrogen production, making it extremely sensitive to electricity prices and lacking economic competitiveness in the current energy system[7−8].

Against this backdrop, methane pyrolysis for hydrogen production offers strong potential as a benchmark technology for "blue-green hydrogen" because it avoids CO_2 emissions while producing high-purity H_2 and valuable solid carbon. The process converts methane directly into hydrogen and solid carbon *via* pyrolysis ($CH_4 \rightarrow C(s) + 2H_2$). The primary advantage arises from this reaction pathway is that it circumvents CO_2 formation. The life-cycle carbon intensity is only 6.1−8.3 kg/kg, which is 71% and 46% lower than that of gray hydrogen and blue hydrogen, respectively. Using renewable methane (for example, biogas-derived methane or methane produced by photovoltaic electrolysis) can yield a negative carbon footprint of −1.2 kg/kg[9]. This process also offers clear advantages in energy use and economic viability. Its reaction enthalpy is only 45% of that of steam methane reforming and 26% of the theoretical value of water electrolysis (+286 kJ/mol), and system thermal efficiency can reach 75%–85%[10]. Globally, the levelized cost of hydrogen from methane pyrolysis is approximately \$1.03–2.45 per kilogram of H_2[11], which is substantially lower than the cost of water electrolysis powered by renewables (around \$14.5 per kilogram)[7]. Although this cost can still exceed that of conventional steam reforming (about \$2.1 per kilogram), sales of carbon by-products (such as carbon black and graphene) can offset a substantial portion of expenses and improve overall economic performance. Moreover, the carbon emission intensity of methane pyrolysis (4.2–9.14 kg/kg) is markedly lower than that of steam reforming (10.09–17.21 kg/kg)[11]. The U.S. Department of Energy estimates that converting solid carbon by-products into high-value materials can offset 30%–50% of hydrogen production costs, further enhancing this pathway's economic feasibility[7].

However, methane pyrolysis technology encounters significant challenges, including high reaction temperatures, catalyst deactivation, reactor clogging, and controlling carbon product quality, which hinder its large-scale commercial application[12−14]. To address these issues, research has centered on developing catalysts. Initial studies concentrated on solid catalysts like Ni, Fe and Co, which effectively lower reaction temperatures but tend to deactivate quickly due to carbon buildup and are challenging to regenerate. To overcome the limitations of solid catalysts, liquid catalyst systems have made demonstrated excellent advantages in recent years, such as molten metals (e.g., Ni-Bi alloys) and molten salts[15−16]. These liquid media offer both catalytic and heat transfer capabilities, facilitating the continuous separation of carbon products and providing a groundbreaking solution for enhancing the process's continuity and efficiency.

With the rapid advancement of the hydrogen energy economy, current methane cracking technologies primarily focus on two main pathways including solid catalytic decomposition and molten medium catalytic. These methods exhibit notable differences in their reaction mechanisms and engineering challenges. In this paper, the catalysts used in conventional methane cracking are first reviewed, specifically those involving solid metal and carbonaceous catalysts. Then, the most significant and recent developments in methane cracking using molten media are discussed, which aims to highlight the potential application of molten media catalysis in methane cracking systems to achieve cleaner, more efficient hydrogen production and carbon product recovery.

1 Solid catalytic systems

Solid catalysts are crucial in catalytic reactions because of their high efficiency and ease of separation. However, their industrial applications are significantly constrained by deactivation phenomena such as coking and sintering[17]. In methane pyrolysis for hydrogen production, solid catalysts can effectively lower the reaction temperature and enhance reaction efficiency; nonetheless, they encounter challenges such as the coverage of active sites and reactor blockage resulting from carbon deposition. Current research aims to improve the anti-coking ability and long-term operational stability of catalysts while simultaneously enhancing their activity and selectivity. This is achieved through precise regulation of the geometric and electronic structures of active sites, optimization of support properties, construction of alloy systems, and management of the carbon-catalyst interface. Furthermore, the research explores controllable synthesis and efficient separation methods for various carbon product morphologies.

1.1 Carbon-based solid catalysts

Carbon-based solid catalysts hold significant research importance in methane catalytic cracking due to their abundant precursor resources, cost-effectiveness, and

exceptional thermal stability[18−20]. Importantly, these catalysts inherently resist sulfur components like H_2S in methane, which typically cause irreversible deactivation in metal catalysts. This resistance eliminates the need for pre-desulfurization in traditional metal catalytic systems, thereby enhancing their suitability for processing sulfur-containing feed gases. Moreover, in carbon-based catalytic systems, carbonaceous deposits formed during reactions can transform into new active sites through *in situ* activation, demonstrating distinctive autocatalytic properties[12].

The activity and stability of solid carbon materials as catalysts for methane pyrolysis are primarily influenced by two factors: the atomic-scale electronic/geometric structure and the macroscopic pore structure. At the atomic level, catalytic activity arises from unsaturated carbon sites at edges or defects, known as high-energy sites[12−14,21−22]. Muradov et al.[21−22] conducted a systematic comparative study on various carbon materials' catalytic activities. They discovered that disordered (amorphous) carbon materials, such as activated carbon (AC) and carbon black (CB), exhibit significantly higher catalytic activities than highly ordered carbon materials like graphite, diamond and carbon nanotubes. This increased activity is attributed to the abundance of high-energy sites in disordered carbon materials, including crystal edges, defects, and dangling bonds. Muradov et al.[21] also observed that upon contact with hydrocarbons, CB transitions from a randomly oriented structure to a more ordered turbostratic structure, with an interplanar spacing (*d*-spacing) of 3.4948 Å between amorphous carbon and pure graphite. This ordering is linked to a reduction in catalytic activity, suggesting that defect sites are the active centers for catalytic reactions. Thus, catalytic activity is inversely related to the crystallinity of carbon, with amorphous carbon being more active than turbostratic carbon, which in turn is more active than graphite. Wang et al.[13] utilized the full width at half-maximum of the C 1*s* peak in X-ray photoelectron spectroscopy to assess carbon defect concentrations. This concentration is positively correlated with the initial reaction rate, reaffirming that the defect sites serve as the active centers for catalytic reactions.

Although high initial activity is impressive, it does not guarantee long-term stability. The sustained activity of catalyst largely relies on its physical structural properties, such as specific surface area and pore structure. Muradov et al.[21] observed that although AC exhibits a high initial activity (e.g., coacervate AC has an initial rate of up to 1.76−1.90 mmol/(min·g)), its numerous micropores with an effective pore size of 25−32 Å are prone to clogging by large carbon crystals (>100 Å) formed during methane decomposition. This clogging leads to a rapid decline in surface area and, consequently, quick deactivation. In contrast, most of the CB surface is "open" and easily accessible, resulting in a slower decay of surface area and more stable catalytic performance[21]. The properties of various carbon materials such as disordered microporous carbon, mesoporous carbon, ordered mesoporous carbon, and nonporous carbon nanotubes were also compared. Although mesoporous carbon initially shows the highest activity, its pore channels quickly become deactivated due to the rapid clogging by deposited carbon. In contrast, ordered mesoporous carbon, with uniformly large pore size of ~3.5 nm, offers moderate initial activity but provides ample space for carbon deposits within its regular pore system. This structure allows ordered mesoporous carbon to maintain stable catalytic activity over a longer duration, ultimately achieving the highest cumulative hydrogen production of 143 mmol/g[19]. The study highlights that an ideal carbon catalyst should combine a high defect concentration for abundant active sites with a well-developed, regular mesoporous system to resist deactivation from carbon deposition.

The synergy between carbon materials in composites has shown a significant catalytic effect. Yang et al.[18] examined the enhanced performance of methane decomposition using both AC and CB. While AC exhibits high initial activity, it deactivates quickly, on the other hand, CB offers stability and autocatalytic properties despite its lower initial activity. When mixed in various ratios, the $AC_{0.5}CB_{0.5}$ composite demonstrated optimal catalytic stability at 900 °C. The initial high activity was attributed to AC, whereas CB contributed to long-term stability. Characterization revealed that on AC, the carbon was mostly amorphous and prone to pore clogging, leading to deactivation. In contrast, on the hybrid AC/CB catalyst, CB altered the morphology and structure of the deposited carbon, where the carbon was more graphitized with curved graphene layers and structural defects (e.g., edges, dangling bonds), creating new active sites for methane decomposition and delaying deactivation.

While composite strategies can enhance the performance of carbon-based catalysts, their low intrinsic activity remains a significant barrier to widespread application[12,19,21−22]. Experimental data indicate that the methane decomposition rates (0.22−2.04 mmol/min·g) for various carbon materials (e.g., AC, CB) generally fall short compared to those of metal catalysts, such as loaded Fe catalysts, achieving up to 1.7−2.9 mmol/(min·g) Fe under identical conditions at 850 °C. This inherent activity disadvantage typically necessitates higher reaction temperatures for carbon-based catalysts to match the methane conversion rates, inevitably increasing both energy consumption and process costs.

1.2 Metal-based solid catalysts

Solid metal catalysts are crucial in methane catalytic decomposition (CDM) for hydrogen production, as they lower the activation energy required to break C−H bonds, allowing reactions to occur efficiently at relatively low temperature. The intrinsic activity of methane catalytic decomposition follows a specific order: Ni, Co, Ru, Rh > Gt, Pt, Re, Ir > Gt, Pd, Cu, W, Fe, Mo[14]. Among these, transition metals like Ni, Co and Fe are particularly

promising due to their low cost and high activity caused by the unfilled 3*d* electronic orbitals[23−24].

The primary challenge for unloaded catalysts is their rapid deactivation caused by metal particle sintering and carbon encapsulation[25]. Alloying strategies have proven effective in tackling this problem. For instance, Cunha et al.[26] incorporated Cu into a nickel catalyst to create a nickel-copper alloy. This modification changed the carbon deposition pathway, favoring the formation of carbon nanofibers or multi-walled carbon nanotubes, which effectively prevents the development of carbon inclusions responsible for deactivation. The study by Lua et al.[27] expanded alloying into the ternary system, creating carrier-free ternary alloy catalysts by thermally decomposing a Ni-Cu-Co oxalate precursor. They discovered that adding Co significantly enhanced the structural stability at high temperature, such as 750 °C, while suppressing the quasi-liquid phenomenon common in Ni-Cu alloys. However, excessive Co content led to phase separation, negatively affecting catalytic activity. Wang et al.[28] confirmed the benefits of alloying in loaded systems, demonstrating that the Ni-Fe/Al_2O_3 catalyst maintained its activity at 923 K for 210 h of continuous reaction at an optimal Fe doping ratio (Ni/Fe/Al = 2∶1∶1). The carbon yield reached 562 g/g, attributed to the great ability of Ni-Fe alloy phase to balance the diffusion rate of carbon atoms within the metal body phase and the generation rate of carbon atoms at the surface.

Carrier engineering and metal-carrier interactions play a crucial role in catalyst performance, as demonstrated by Lim et al.[29]. They compared the performance of nickel loaded on dendritic fiber nanosized SiO_2 (KCC-1) with that on conventional Stöber SiO_2. The study revealed that the special morphology of KCC-1 facilitates the formation of more thermodynamically stable 2∶1 Ni-paged silicates with nickel species, thereby causing highly dispersed Ni particles (2.5−4.5 nm) with improved sintering resistance by strong metal-carrier interactions. This strong interaction enhances intrinsic activity, with an initial hydrogen yield of 0.3 mol/(g·h) at 500 °C for Ni/KCC-1, it also intensifies carbon encapsulation during the reaction. This encapsulation alters the growth mode of carbon nanotubes from the typical tip-growth observed on Ni/SiO_2 to base-growth (illustrated in Figure 1(b))[30]. Similarly, as illustrated in Figure 1(c), Xue et al.[30] precisely controlled metal-support interaction(MSI) by constructing a core-shell structure. They synthesized SiO_2-loaded Ni nanoparticles and enveloped them with a nanometer-thick TiO_2 shell, forming the embedded core-shell structure as depicted in Figure 1(c)[31]. This design not only stabilizes the Ni nanoparticles by geometrically confining the domains and preventing their deactivation by carbon nanotubes (CNTs) "pulling out" through the tip growth mechanism, but it also facilitates reactant mass transfer and provides space for CNT growth through the porous TiO_2 shell. In addition, research indicates that carriers with varying properties also can direct the carbon growth path *via* distinct mechanisms. For instance, when MgO serves as the support, its basic characteristics and lattice structure facilitate the formation of robust interaction phases, such as NiO-MgO solid solutions or magnesium ferrite (Fe_2MgO_4), with active metal precursors (Ni or Fe) at elevated temperatures[32]. This bonding at the "bulk" scale not only stabilizes metal nanoparticles and inhibits their sintering at high temperatures but also fundamentally predefines the assembly path of carbon atoms. Specifically, multi-walled carbon nanotubes predominantly form on Ni/MgO, while few-layer graphene sheets uniquely develop on Fe/MgO. This observation underscores the capacity of the support to directly dictate the dimensions and macroscopic morphology of carbon products through bulk chemical bonding. In contrast, when Al_2O_3 is employed as the support, its mechanism of action emphasizes "interface engineering". A systematic study by Yang et al.[33] demonstrated that in the Ni/Al_2O_3 catalyst, the yield of carbon nanotubes is positively correlated with the presence of a specific β_2-type NiO species, which serves as a strong interaction site associated with the Al-rich mixed oxide phase.

Kutteri et al.[34] systematically investigated SiO_2-loaded bimetallic catalysts to explore the relationship between alloying and carbon product morphology. They discovered that bimetallic catalysts like 9Ni-1Fe/SiO_2 and 9Ni-1Co/SiO_2 not only reduced metal grain size through the formation of alloying phases such as Ni-Fe and Ni-Co, but also enhanced catalytic performance *via* electronic effects. This resulted in methane conversion rates of up to 60% and carbon production of up to 2.5 g/g at 650 °C. Significantly, they demonstrated that the Ni-Fe/SiO_2 catalyst predominantly produces fishbone carbon nanotubes with a tip growth mode. In contrast, the Fe/SiO_2 catalyst selectively synthesizes substrate-growing carbon nanotubes at 700 °C, maintaining this growth characteristic even after regeneration. This finding offers a novel approach for catalyst recycling. Additionally, hydrotalcite derived catalysts hold significant promise in CDM research due to the distinctive layered structure and "memory effect". Sikander et al.[35] conducted a systematic study on the Mg-Ni-Al hydrotalcite system, revealing that nickel content critically influences performance. At a Ni content of 40% (exLDH-Ni40), the catalyst achieved optimal performance, maintaining approximately 80% methane conversion for up to 6 h at 650 °C. This impressive performance is attributed to the formation of spinel-like structures, such as (Ni, Mg)Al_2O_4, upon calcination at 850 °C. XRD and H_2-TPR characterization confirmed that this structure effectively anchors nickel species, preventing migration and sintering. It also facilitates the uniform growth of carbon nanofibers (CNFs), ensuring that active Ni^{3+} sites remain exposed at the fiber tips to continuously catalyze the reaction. Similarly, the complex role of cobalt in $Co_{3-x}Al_xO_4$ (x=0−2) catalysts was explored by Calgaro & Perez-Lopez[36]. When the Co/Al molar ratio ranges from 1 to 2.3, the catalysts exhibit hydrotalcite-like properties, characterized by a high specific surface area and excellent cobalt dispersion. TPR analysis identified up to six reducible phases, including the

Co_3O_4 bulk phase and various $Co_{3-x}Al_xO_4$ mixed oxides. The reduction temperatures of these phases increased with higher Al content, indicating stronger interactions between the oxides with the carrier. Although these catalysts show optimal activity and stability at 500 °C, the deactivation pathway is highly dependent on the activation method, where high-temperature reduction in H_2 at 700 °C often leads to sintering, while *in situ* activation in CH_4 primarily causes deactivation due to the deposition of amorphous carbon.

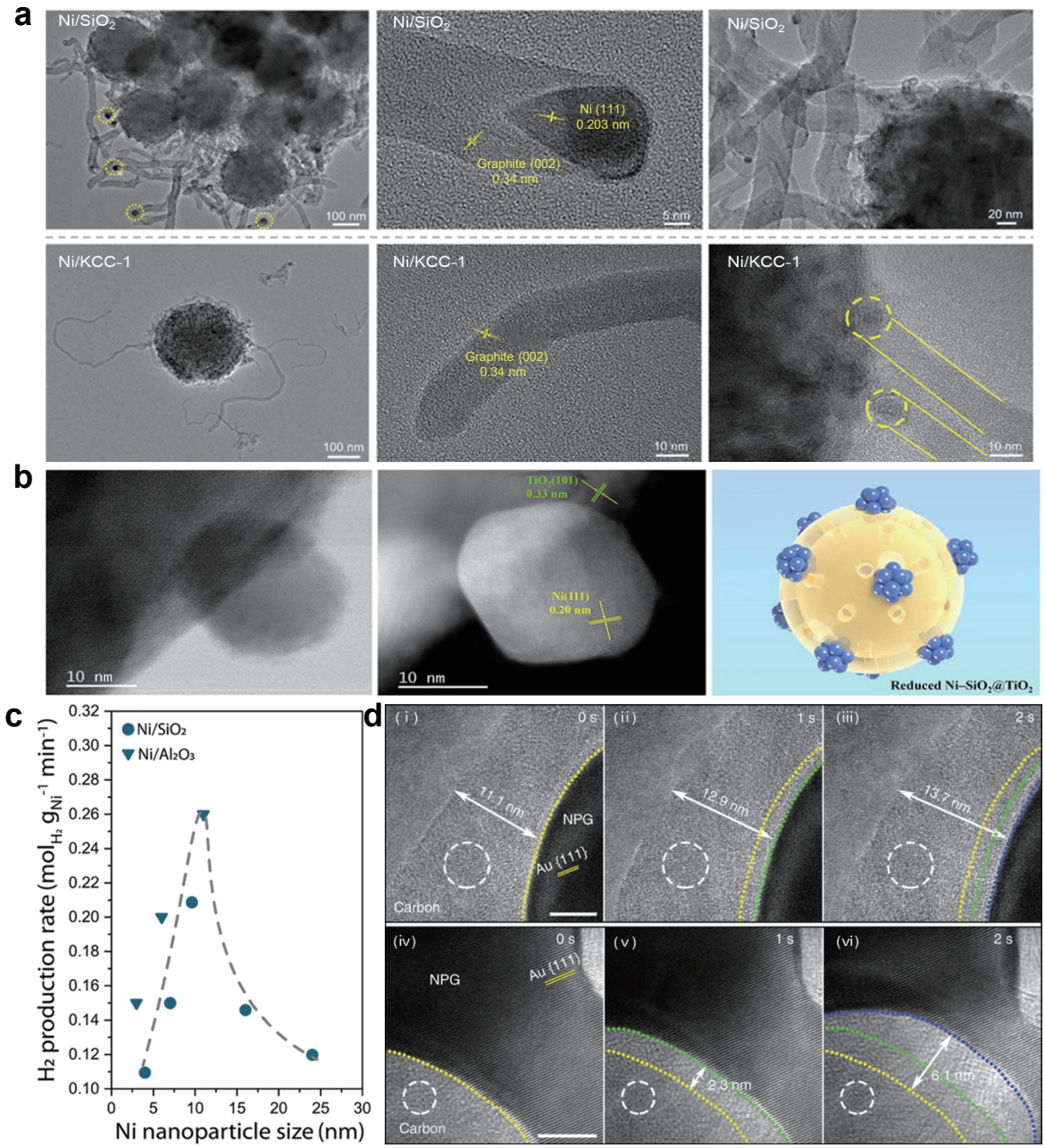


Fig. 1 (a) Schematic illustration of substrate and tip growth modes for carbon nanotubes[29]; (b) Schematic depiction of the core-shell structure of the 8Ni-SiO_2@10TiO_2 catalyst, accompanied by a HAADF-STEM image showing Ni nanoparticles partially encapsulated by the TiO_2 shell[30]; (c) Evolution of the metal-specific hydrogen production rate, with the average Ni^0 nanoparticle diameter in the activated catalyst, i.e. following reduction, for a series of Ni/SiO_2 and Ni/Al_2O_3 supported catalysts with monomodal Ni particle size distributions[31]; (d) i−iii HRTEM images at three different moments during the reaction on a surface region with positive curvature (The images have the same scale bar. The moment in i is defined as 0 s. The yellow, the green, and the blue dashed lines indicate the positions of the surface at 0, 1 and 2 s, respectively. The white dashed circles denote the positions of a randomly selected carbon region, and the arrows indicate the thickness of the amorphous carbon at 0, 1 and 2 s) and iv−vi have the same meanings as i−iii but are for a surface region with negative curvature[37]
(with permission from ACS Publications, Elsevier and Springer Nature)

The performance of metal catalysts depends not only on their composition and supports but also on the dynamically evolving carbon-metal interface that forms during reaction. Recent works have shown that the initial size of metal nanoparticles is a critical structural determinant of the interface and the catalyst's fate. Atashi et al.[31] systematically examined Ni/SiO_2 and Ni/Al_2O_3 and found that the mass-specific hydrogen production rate follows a volcano-shaped dependence on Ni particle size, with a maximum when the particle size is near 10 nm (Figure 1(c)). This optimal size reflects control over the carbon growth mode: Ni particles below 10 nm are readily encapsulated by an initial thin layer of amorphous carbon and thus deactivate quickly, becoming "non-productive" particles; particles larger than this threshold act as stable nucleation sites, sustain tip-growth of CNFs and remain "productive" , preserving hydrogen production activity. This size threshold reflects the minimum energetic and geometric requirements for graphite carbon fiber nucleation. Crucially, the carbon-metal interface is dynamic during the reaction. Carbon species from methane cracking actively interact with and restructure the metal catalyst. Operando XRD and DFT calculations show that adsorbed species such as C and CH_3, formed in the reaction's initial stage, markedly lower the energy barrier for Ni atoms to detach from surface defect sites on nanoparticles. This effect drives carbon-induced, reaction-driven migration of metal atoms and Ostwald ripening, producing pronounced reorganization and growth of catalyst metal particles under working conditions. Thus, the observed catalytic activity arises from the combined influence of the initial metal size distribution and the dynamic sintering behavior during the reaction. The dynamics of the carbon-metal interface extend beyond transition-metal catalysts. Xi et al.[37] used *in situ* TEM to show that, during catalytic methane pyrolysis by nanoporous gold, the gold surface continuously disintegrates and releases Au single atoms (Figure 1(d)). These atoms disperse into the forming amorphous carbon matrix and co-catalyze the reaction alongside the host NPG. Further observations show that the dispersed Au single atoms reversibly aggregate into nanoparticles within the carbon layer and then dissociate, establishing a co-catalytic system in dynamic equilibrium of "single atoms ↔ nanoparticles". DFT calculations indicate that adsorption of reaction intermediates (for example, CH_3*) on Au clusters weakens metal-metal bonds and facilitates this dissociation. The study therefore demonstrates that the carbon product layer can act as a dynamic carrier for metal active sites and that the metal state at the interface (single atoms or nanoparticles) depends on the carbon deposition microenvironment and the reaction conditions.

In summary, the performance of solid metal catalysts is governed by the active-site structure, support properties, alloy composition, and the dynamic carbon-metal interface that forms during reaction. Coke deposition is not merely an end-stage deactivant but constitutes an active interfacial phase. This phase actively reshapes the catalyst in real time and redirects reaction pathways. Controlling the dynamic interface—by stabilizing the initial metal's size and state through alloying and support design, and by using the carbon layer to tune the dispersion and electronic state of metal sites—is therefore critical for achieving high activity, long-term stability, and selective synthesis of high-value carbon materials.

2 Molten media system (MMC)

Molten media-catalyzed methane pyrolysis technology optimizes catalytic activity, heat transfer, and carbon product separation by creating a liquid reaction interface. Unlike solid catalysts in fixed-bed reactors, the molten medium offers a dynamic reaction surface, preventing catalyst deactivation caused by carbon deposition. It also promotes uniform heat distribution and transfer, ensuring reaction stability. Based on catalytic media, MMC fall into two categories including molten salt catalysts and molten metal/alloy catalysts. The physical properties of common metals are listed in Table 1, and the catalytic performance of these molten media is summarized in Table 2. At present, MMC predominantly appiled in bubbling tower reactors, as shown in Figure 2(a)[38], which can leverage the gas-liquid interface for efficient mass transfer and reaction.

2.1 Catalytic mechanism in MMC

The mechanism of methane pyrolysis in molten catalysts primarily involves the interaction between bubble dynamics and interfacial reactions. In this process, methane gas is introduced into the molten medium (metal or salt) as bubbles. Subsequently, pyrolysis reaction occurs ($CH_4 \rightarrow C(s) + 2H_2$) as these bubbles rise. During the methane pyrolysis process, the bubble-melt interface serves as the primary reaction site, while the gas-phase reaction within the bubble plays a minor role. Numerical simulations by Mehrabian et al.[39] demonstrate that methane pyrolysis is predominant at this interface by solving the energy and mass conservation equations:

$$\frac{1}{r^2}\frac{\partial}{\partial r}\left(r^2 k_g \frac{\partial T_B}{\partial r}\right) + R_{rxn}\Delta H_{rxn} = \rho c_p \frac{\partial T_B}{\partial t} \quad (1)$$

$$\frac{1}{r^2}\frac{\partial}{\partial r}\left(D_{i,mix} r^2 \frac{\partial C_i}{\partial r}\right) + R_{rxn} = \frac{\partial C_i}{\partial t} \quad (2)$$

where r is the radial coordinate (m), k_g is the thermal conductivity of the gas (W/(m·K)), T_B is the temperature within the bubble (K), R_{rxn} is the reaction rate (mol/(m^3·s)), ΔH_{rxn} is the enthalpy of reaction (J/mol), ρ is the density (kg/m^3), c_p is the specific heat capacity (J/(kg·K)), t is time (s), $D_{i,mix}$ is the diffusion coefficient of species i in the mixture (m^2/s), and C_i is the concentration of species i (mol/m^3).

The calculation results indicate that under typical reaction conditions, over 97% of methane conversion occurs at the

bubble-melt interface, with gas-phase reactions inside the bubble contributing less than 3% (Figure 2(b)). This finding underscores the crucial role of molten catalysts such as $Ni_{0.27}Bi_{0.73}$ by providing active sites at the interface and significantly reducing the activation energy, with 208 kJ/mol of E_a at the interface compared to 422.9 kJ/mol inside the bubble[39].

The size, frequency, and increasing rate of bubbles significantly affect both the residence time of methane and the gas-liquid interface area, thus determining the conversion rate. Sun et al.[40] utilized the differential pressure transmitter (DPT) technique to analyze bubble characteristics in high-temperature molten tin and LiCl-KCl systems. By comparing bubble diameters measured by DPT with values predicted by empirical correlation equations, such as those by Jamalahmadi and Gaddis-Vogelpohl, they found that the deviation was less than 8% (e.g., approximately 5% in molten tin). This result confirms the reliability of the DPT technique for characterizing bubbles in high-temperature opaque systems. The bubble volume can be calculated using the following formula:

$$V_B = \frac{V_{G,Z}}{f_B} \quad (3)$$

where V_B is the volume of a single bubble (m^3), $V_{G,Z}$ is the gas volume flow rate (m^3/s) and f_B is the bubble frequency (s^{-1}). The study also highlighted the critical role of gas preheating. Without adequate preheating, the gas temperature during bubble formation falls below the melt temperature, resulting in conversion deviations.

Iguchi et al.[41] investigated bubble characteristics in a 160 °C molten iron bath using an electrical resistivity probe. Their findings showed that the bubble diameters aligned with the empirical equations proposed by Mori et al.[42]:

$$d_B = \left[\left(\frac{6\sigma d_{no}}{\rho_L g}\right) + \left\{0.0242(Q_G d_{no})^{0.867}\right\}^{1/6}\right] \quad (4)$$

where d_B is the bubble diameter (m), d_{no} is the nozzle outer diameter (m), σ is the surface tension (N/m), ρ_L is the melt density (kg/m^3), g is the gravitational acceleration (9.81 m/s^2), and Q_G is the gas flow rate (m^3/s)[41]. Experiments indicate that raising the temperature from 125 to 160 °C reduces the bubble frequency while increasing the diameter, thereby influencing the renewal rate of the reaction interface.

In this interfacial reaction-dominated mechanism, operating parameters significantly influence the conversion rate by altering the interfacial area and the transfer process. Among these factors, melt temperature is the most sensitive because its increase exponentially boosts the interfacial reaction rate. Bubble size is also crucial as reducing the initial bubble radius from 2.6 to 0.6 mm can enhance the conversion rate by approximately 12% by increasing the surface area-to-volume ratio and extending the residence time[39]. Conversely, increasing system pressure from 0.1 to 8 MPa strongly inhibits conversion, causing the final conversion to drop sharply from over 80% to ~20%. This is primarily due to the Le Chatelier principle, as high pressure diminishes gas diffusion to the interface. The intrinsic physical properties of the melt such as surface tension and density fundamentally influence the kinetic behavior of bubbles. Computational fluid dynamics simulations conducted by Okajima et al.[43] demonstrate that, bubbles are prone to deformation and can even transition into a jet state in NaBr-KBr molten salts that have low surface tension, significantly enlarging the gas-liquid interfacial area. In contrast, in Fe and Al melts, bubbles maintain more regular shapes. These findings indicate that selecting an appropriate melt medium to control bubble dynamics is crucial for optimizing reactor performance.

Methane pyrolysis in molten catalysts primarily relies on interfacial reactions, with bubble kinetics and molten catalysts jointly influencing reaction efficiency. By strategically optimizing gas injection rate, system factors, and melt selection, the interfacial area and residence time can be maximized, and then significantly boosting hydrogen yield.

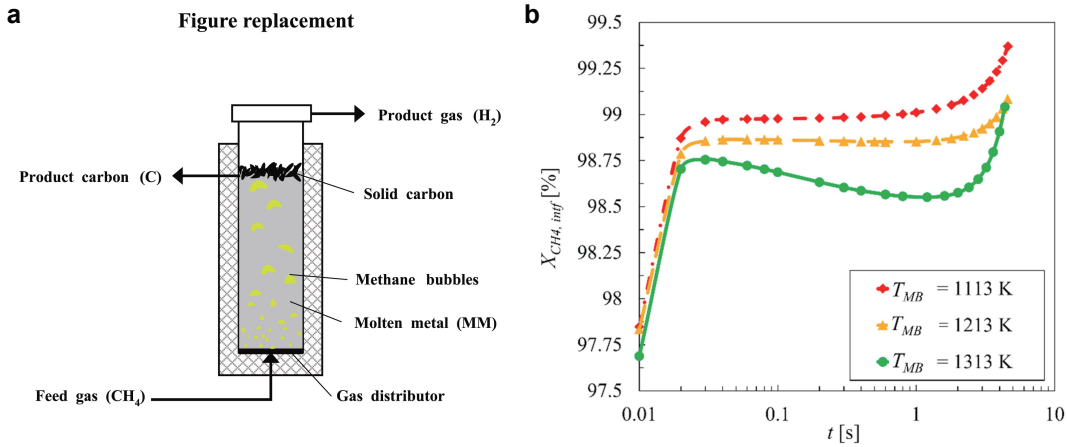


Fig. 2 (a) Schematic diagram illustrating a typical bubbling apparatus[38]; (b) Percentage of methane consumption at the bubble interface with the molten $Ni_{0.27}Bi_{0.73}$ bath across various molten bath temperatures[39] (with permission from Elsevier)

2.2 Progress in molten medium catalytic research

2.2.1 Liquid metal monomer catalysts

Previous research has investigated the use of various low melting point metals in methane pyrolysis, revealing significant differences in catalytic activity, operational stability, and carbon separation. Wang et al.[44] were pioneers in demonstrating the catalytic role of molten Mg, though its volatility at high temperatures restricted its application. Geißler et al.[45] showed that molten Sn at 1175 °C achieved a 78% hydrogen yield. However, its primary function was as an efficient heat transfer medium rather than a catalyst as carbon primarily accumulated on its surface without catalytic activation. In contrast, Pérez et al.[46] achieved a 91% methane conversion using molten Ga at 1119 °C, demonstrating that Ga possesses both excellent catalytic activity and thermal transfer properties. Upham et al.[47] also reported promising results using molten Ni-Bi alloys. Additionally, Zeng et al.[48] discovered that liquid Te not only serves as an effective catalyst but also exhibits catalytic activity in its vapor form, offering new insights into the reaction mechanism at the gas-liquid interface.

The catalytic activity of liquid metals is intricately linked to their electronic structures. This connection is further evidenced by Zeng et al.'s study on Te[48], which attributes the remarkable ability of Te to catalyze C−H bond breaking in methane to its high electron affinity and electronegativity. Interestingly, the catalytic activity is reduced after adding Ni to Te, which contrasts with the "Ni potentiation" effect seen in solvents like Bi and Sn[45,47]. This indicates that catalytic activity is influenced not just by the active atoms themselves but also by their electronic microenvironment within a specific liquid metal solvent.

2.2.2 Liquid alloy catalysts

Selecting the appropriate catalyst is essential for optimizing reaction efficiency and stability of methane pyrolysis. Traditional high-activity transition metal catalysts such as Ni and Fe effectively convert methane at moderate temperatures. However, the solid-state properties and significant carbon buildup at elevated temperatures often result in rapid deactivation and reactor clogging. Conversely, metals with low melting points, like Sn, Bi and In, remain liquid at reaction temperatures, offering a favorable interface for carbon precipitation and reducing deep carbon accumulation. Despite this advantage, their inherent catalytic activity is typically low, limiting overall reaction efficiency[47]. Table 1 presents the physical properties of metallic elements frequently employed in methane pyrolysis. The highly active transition metals such as Fe, Ni and Co typically possess melting points exceeding 1450 °C. In contrast, post-transition metals like Sn, Bi, In and Ga, which serve as solvent metals, exhibit much lower melting points, generally below 700 °C. Notably, Ga stands out with a melting point of just 29.7 °C, allowing it to remain liquid at near room temperature, thus enabling the development of low-temperature reaction systems. To address the "trade-off" between activity and stability, researchers are exploring the alloying of highly active metals with low melting point metals to create liquid alloy catalysts, which represents a promising research avenue.

Table 1 Physical properties of common metals used for CH_4 pyrolysis[15,49]

Category	Metal	Melting point/°C	Boiling point/°C	Density/(g·cm^{-3}) at STP*	Specific heat /(J·kg^{-1}·K^{-1})	Thermal conductivity /(W·m^{-1}·K^{-1})	Surface tension at melting point*/(mN·m^{-1})	dγ/dT /(mN·m^{-1}·K^{-1}) *
Transition metals	Fe	1538	2862	7.87	449	90	1862 (1909)	−0.39 (−0.52)
	Ni	1455	2730	8.91	445	91	1786 (1834)	−0.35 (−0.376)
	Cu	1084.6	2562	8.93	384.4	400	1336 (1374)	−0.26 (−0.26)
	Pd	1554.9	2963	12.02	244	71.8	–	–
	Pt	1768.3	3825	21.45	133	71.6	–	–
	Co	1495	2927	8.86	421	100	1831 (1922)	−0.34 (−0.44)
Alkaline earth metal	Mg	650	1091	1.74	1020	160	567	−0.36
Metalloid	Te	449.5	988	6.23	201	3	239	−0.104
Post-transition metals	Pb	327.4	1740	11.34	130	35	468 (471)	−0.11 (−0.159)
	Bi	271.5	1564	9.8	122	8	382 (383)	−0.080 (−0.097)
	Sn	231.9	2602	7.28	217	67	552 (586)	−0.105 (−0.124)
	In	156.6	2072	7.31	233	82	556 (561)	−0.090 (−0.095)
	Ga	29.7	2400	5.91	371	29	711 (724)	−0.070 (−0.072)
	Zn	419.5	907	7.14	388	116	789 (817)	−0.21 (−0.227)
	Al	660.3	2470	2.7	897	237	871 (890)	−0.155 (−0.182)

*Note: STP: standard temperature and pressure (0 °C, 1 atm). Values in parentheses for surface tension (mN/m) and dγ/dT (mN/(m·K)) are given at the melting point of the respective metal. Data are compiled from the references.

The groundbreaking research by Upham et al.[47] successfully demonstrated the full feasibility of this concept by developing a Ni-Bi liquid alloy bubble column reactor (Figure 3). The primary advantage of this system is the dynamic gas-liquid interface, which continuously expels solid carbon, effectively addressing the rapid deactivation of conventional solid-state catalysts caused by carbon buildup. In this setup, Ni atoms dissolved in liquid Bi serve as catalytic active sites, achieving 95% methane conversion at 1065 °C and maintaining stable operation for over 170 h. The carbon produced forms highly graphitized flakes (I_D/I_G = 0.594) that float on the melt surface due to their lower density, so facilitating easy separation. Notably, theoretical simulations indicate that the active metal Ni is atomically dispersed and negatively charged within the liquid Bi, with its charge distribution closely linked to catalytic activity, revealing the atomic-scale nature of the liquid alloy catalysts. To further enhance the local electronic environment of the active sites, researchers have begun introducing a third metal element. For example, in the NiMo-Bi ternary alloy developed by Chen et al.[16], the introduction of Mo diminished the "caging effect" of Bi on Ni active site. This alteration increased the XPS binding energy of Ni from 852.2 to 852.5 eV, bringing it closer to the zero valence state of metal. Consequently, the methane C−H bond activation energy was reduced to 81.2 kJ/mol, achieving a 16.3% methane conversion at 800 °C, and operating stably for 120 h without deactivation.

In recent years, the descriptor-driven rational design approach has emerged as a new paradigm for developing liquid alloy catalysts. Han et al.[50] systematically analyzed the catalytic behavior of Bi-based binary alloys (M = Ni, Pt, Cu and Ag) by integrating density-functional theory with ab initio arithmetic molecular dynamics simulations (Figure 4 (a), (b)). They identified two key descriptors, in which the H* formation energy indicates the methane dissociation adsorption energy barrier, and the solute-metal diffusion coefficient reflects the exposure of active sites at the dynamic bubble interface. Utilizing these descriptors, the researchers successfully predicted and validated that both $Bi_{68}Ni_{27}Cu_5$ and $Bi_{68}Ni_{27}Mn_5$ are ternary alloys with excellent properties. Both alloys achieved a methane conversion rate of 42% at 104 °C, outperforming the 38% conversion rate of $Bi_{73}Ni_{27}$. Notably, the Cu-containing system maintained good stability for 40 h, whereas the Mn-containing system gradually deactivated after 20 h due to the carbonization of Mn. Kim et al. [51] explored the methane activation process over Zn-Bi alloy catalysts using advanced ab initio molecular dynamics and metadynamics simulations. Their findings revealed that methane dissociation favors the "surface stabilization" pathway, where reaction intermediates form stable bonds with surface atoms instead of producing freely diffusing methyl radicals. Notably, the simulations indicate that Zn does not serve directly as the active site for C−H bond dissociation. Instead, it indirectly aids the reaction by modulating the electronic state (charge rearrangement) of adjacent Bi atoms.

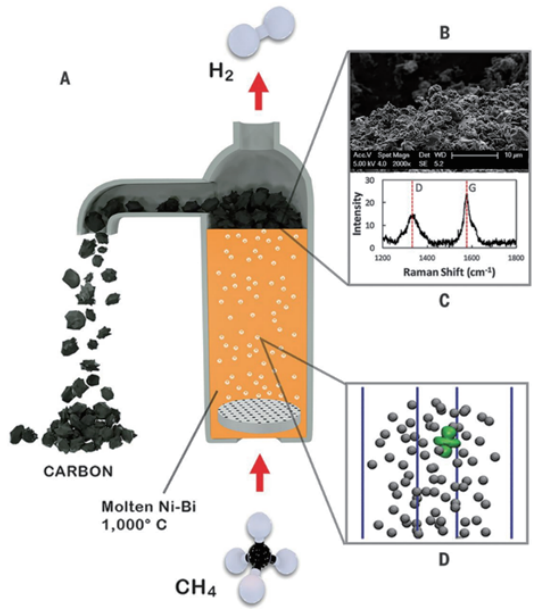


Fig. 3 The paradigm of catalytic methane pyrolysis in a molten metal bubble column reactor[47]
(with permission from AAAS Publications)

This insight challenges the conventional notion that "highly reactive metals must be used as direct active sites" and offers a novel approach for designing catalysts with non-precious metals.

Beyond the intrinsic activity of active sites, the physical properties of the gas-liquid interface critically influence the mass transfer efficiency and reaction rate of reactants. Parameters like surface tension and density of the molten catalyst directly impact the size, distribution, and residence time of reaction bubbles, consequently affecting the total conversion rate. In the study of Cu-based binary alloys, Scheiblehner et al.[52] found that Cu-Bi alloys, particularly the $CuBi_{80}$ system, produced smaller bubbles (~9.676 mm in diameter) mainly due to the low surface interfacial tension, leading to a methane conversion rate of 68.44% at 116 °C, significantly surpassing other Cu-based alloys. These findings indicate that optimizing bubble behavior by reducing surface tension effectively enhances reaction efficiency. To actively regulate interfacial properties, Son et al.[53] conducted a systematic investigation on the interfacial promoting effect of Se in the Ni-Bi system. As illustrated in Figure 4, the promotional effect arises from two primary factors. First, Se enrichment on the surface markedly decreases the alloy's surface tension (Figure 4(c), (d))[53]. Second, an optimal Se amount enhances the interfacial composition, nearly doubling the density of Ni active sites on the surface (Figure 4(e)). Consequently, adding 1% Se to $Ni_{27}Bi_{73}$ significantly lowered the surface tension from 389 to 317 mN/m, reduced the bubble diameter by approximately 6%, and increased the bulk specific surface area. These physical changes, combined with the chemical effect of increasing the surface Ni sites density from 0.00124 to 0.00242 atom/Å^2, significantly boosted the methane conversion of the $Ni_{27}Bi_{72}Se_1$ catalysts from 46.97% to 64.00% at 100 °C.

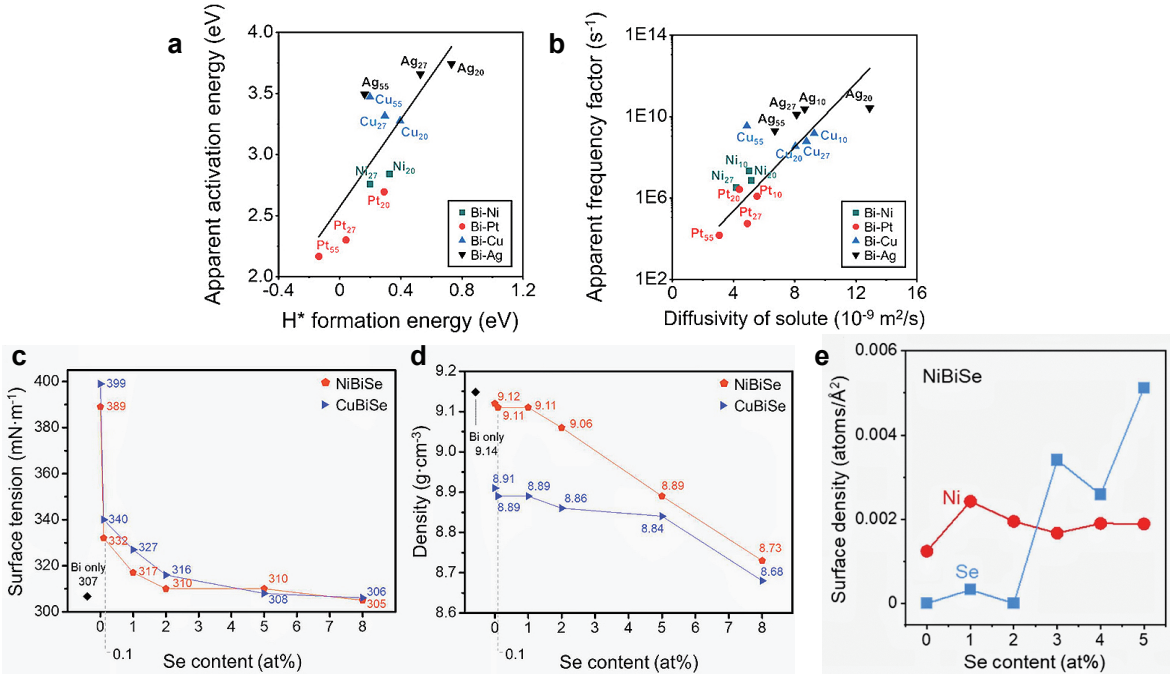


Fig. 4 (a), (b) Descriptors of the catalytic activity of the Bi-M alloy systems[50]; (c), (d) The surface segregation of Se significantly reduces the surface tension of the alloy[53]; (e) An optimal amount of Se maximizes the surface density of Ni active sites by modifying the gas-liquid interface[53]
(with permission from ACS Publications, Elsevier)

The apparent activation energy also decreased from 219.2 to 201.2 kJ/mol and remained stable over the 100 h. Theoretical calculations revealed that adding a moderate amount of Se optimized the local electronic environment of the Ni active site by adjusting the electronic interactions at the interface. However, when Se content exceeded 1%, the excess Se covered the surface active sites, reducing Ni surface density and catalytic activity. This study suggests that adjusting bubble behavior and active site exposure by introducing low-surface-tension elements is an effective strategy to enhance liquid alloy catalyst performance.

In summary, liquid alloy catalysts effectively combine the high activity of solid catalysts with the dynamic interface and ease of separation found in liquid media by dissolving highly active metals, such as Ni and Fe, in low melting point media like Bi and Sn. The catalytic performance depends on the intrinsic properties of the active sites, including their electronic structure, and the mass transfer efficiency, which involves bubble behavior. These factors can be synergistically optimized through the introduction of multiple alloying and interfacial promoters, such as Se, offering a promising solution for achieving a continuous, efficient, and stable methane pyrolysis process to produce hydrogen.

2.2.3 Molten salt catalysts

Molten salts serve as effective catalytic media for methane pyrolysis, which offering the distinct benefits of continuously renewing the reaction interface, preventing carbon buildup deactivation, and facilitating the easy separation of carbon products through density differences or water washing. While pure alkali metal halides (such as NaCl-KCl) exhibit low catalytic activity, incorporating transition metal salts (like Fe, Mn and Cu chlorides) can generate reactive species with Lewis acidity, reduce the apparent activation energy of methane, thereby significantly enhancing catalytic performance.

Kang et al.[54] demonstrated that incorporating 3% $FeCl_3$ into the NaCl-KCl eutectic salt (NaKCl) substantially lowered the apparent activation energy from 301 to 171 kJ/mol. This adjustment enabled a stable methane conversion of about 9% at 100 °C, with no deactivation observed during continuous operation exceeding 50 h. The increased activity of the system was attributed to the formation of complex ions, such as tetrahedral $(FeCl_4)^-$ ions, which exhibit Lewis acidity. These ions, stable in a reducing atmosphere, accumulated at the gas-liquid interface, enhancing the activation of C−H bonds. In comparison, the $MnCl_2$-KCl system displayed even lower activation energy. At a $MnCl_2$(67)-KCl(33) molar ratio, the apparent activation energy dropped to 161 kJ/mol, achieving methane conversion rates as high as 30% and hydrogen selectivity of 99% at 105 °C[55]. This heightened activity arose from stable tetrahedral $(MnCl_4)^{2-}$ ions in the melt, which, as Lewis acidic species, effectively facilitated the catalytic cracking of methane. Figure 5(a)[56] illustrates that the free energy barrier of the $MnCl_2$-KCl system is significantly lower than that of pure $MnCl_2$ during CH_4 dehydrogenation to C*, confirming its thermodynamic advantage. H−D exchange experiments reveal that the reaction pathway favors the formation of CH_2 intermediates over CH_2 radicals, which

are predominant in gas-phase pyrolysis. This preference accounts for its high hydrogen selectivity and the enhanced production of graphitic carbon[56]. Beyond intrinsic catalytic activity, the physical properties of the molten salt, such as density and surface tension, are crucial for mass transfer efficiency and overall conversion, influencing bubble dynamics. As depicted in Figure 6(b), (c)[54−55], Fe(3%)/NaKCl molten salt exhibits lower surface tension than pure NaKCl due to the concentration of active species at the interface, which leads to smaller bubbles, increasing gas-liquid interfacial area and optimizing reaction efficiency[54].

The molten salt catalyst not only speeds up the reaction but also precisely controls the morphology and structure of the carbon products, facilitating a seamless transition from hydrogen production to the creation of high-value carbon materials (Figure 6). In the Fe/NaKCl system, the reaction yields highly graphitized flaky carbon with a Raman spectral I_D/I_G ratio of approximately 0.53, significantly lower than that of 1.53 for amorphous carbon produced in pure NaKCl (Figure 6(a), (b)). Conversely, in the $MnCl_2$-KCl system, the carbon products are multilayered graphene with a regular lamellar structure and an I_D/I_G ratio of around 0.60 (Figure 6(c), (d))[55]. These highly graphitized carbon products are easy to separate by flotation due to the lower density compared to the molten salt, achieving carbon purity exceeding 93% after water washing. The purity of the carbon products is closely linked to the physicochemical properties of the molten salt. Parkinson et al.[57] identified a negative correlation between carbon purity and ionic spacing of salt, suggesting that the molecular size of the salt influences the salt residue in carbon. This insight aids in selecting a molten salt medium for direct access to high-purity carbon products. More innovatively, designing the reaction microenvironment enables the synergistic growth of multidimensional carbon materials. Zhao et al.[58] developed a bubbling chemical vapor deposition method to synthesize 0D carbon black and 2D graphene using a one-pot approach within a molten salt bubble (Figure 6(e)). They employed NaCl-KCl with 3% $CuCl_2$ as the substrate and used the restricted space inside the bubbles as a micro-reactor at a relatively low temperature of 850 °C. Theoretical calculations indicate that the formed $KCuCl_3$ complex ions can significantly lower the dissociation energy of methane's first C−H bond from 4.66 to 1.74 eV. Within this system, the interior of bubble facilitates the gas-phase reaction to produce CB, while the gas-liquid interface directs the formation of Gr, resulting in 0D−2D composite carbon materials with high electrical conductivity.

Molten salt-catalyzed methane pyrolysis effectively addresses deactivation and separation challenges through its dynamic interface. Transitioning from a pure salt system as the reaction medium to a highly active transition metal catalytic salt system, researchers can significantly reduce energy consumption while precisely controlling the structure and purity of carbon products.

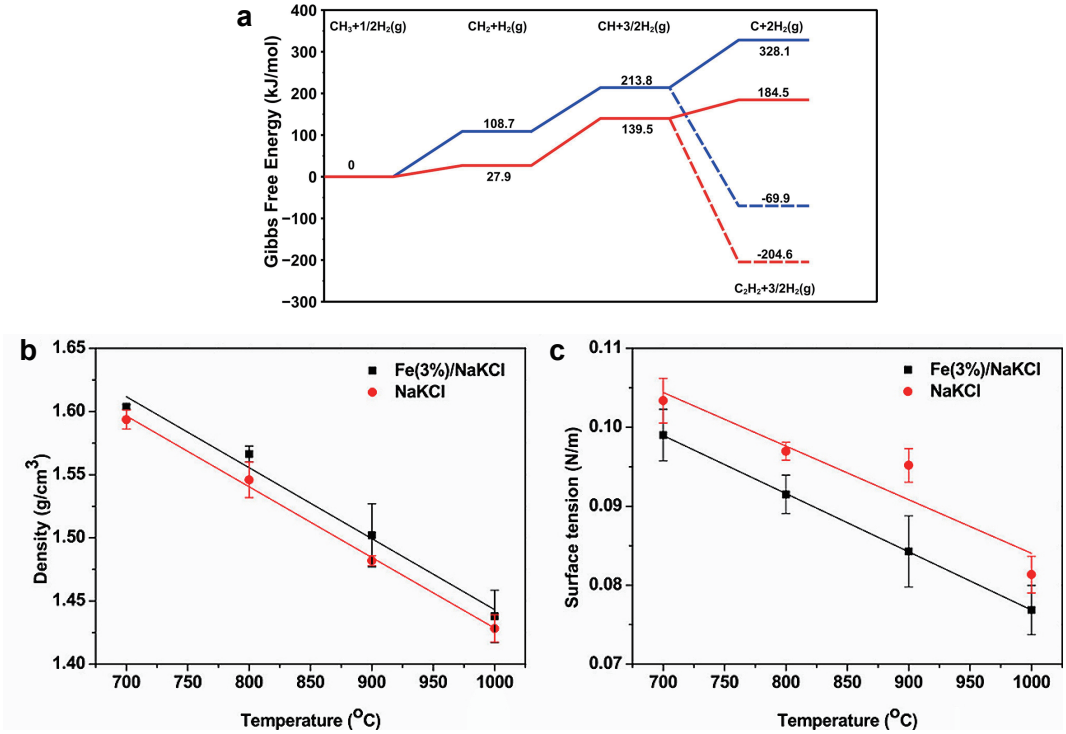


Fig. 5 (a) Gibbs free energy diagrams (at 800 °C) for $CH_4(g)$ to C* + $2H_2(g)$ (solid line) and C_2H_2* formation (dotted line) on $MnCl_2$ (blue) and $MnCl_2$-KCl (red)[56]; Density (b) and surface tension (c) of NaKCl and Fe(3%)/NaKCl molten salt mixtures versus temperature[54]
(with permission from Elsevier, ACS Publications)

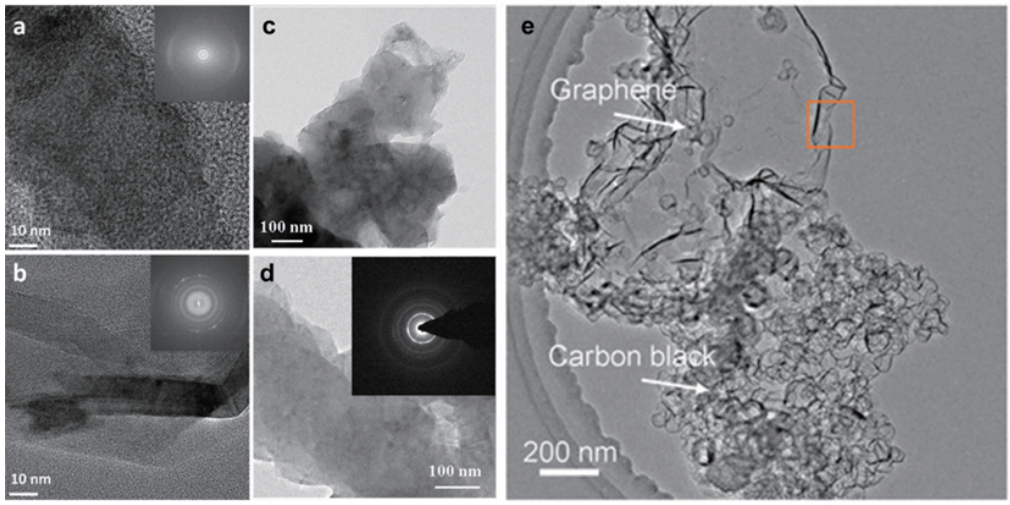


Fig. 6 Comparison of the structure of carbon products generated in different catalytic molten salt systems: (a), (b) Graphite flake layer generated in Fe/NaKCl system (I_D/I_G=0.53)[54]; (c), (d) Multilayer graphene generated in $MnCl_2$-KCl system (I_D/I_G=0.60)[55]; (e) Composite structure of 0D carbon black and 2D graphene synthesized by one-pot method in $CuCl_2$/NaKCl system[58] (with permission from ACS Publications, Elsevier, John Wiley and Son)

Table 2 Summary of the performance of molten metals and molten salt catalysts

Catalyst	Temperature/°C	x_{CH_4}/%	E_a/(kJ·mol^{-1})	Stability/h	Characteristics of carbon products	Reference
Ni_{27}-Bi_{73}	1065	95	208	>170	Graphite sheets	[47]
NiMo-Bi	800	9.87	81.2	120	–	[16]
Cu-Bi_{80}	1160	68.4	–	–	Fine particles containing Bi and Cu impurities	[52]
Sn	1200	~18.3	335.7	–	Loose fibrous	[59]
$SnNi_{20}$	1200	~9.6	204.5	–	–	[59]
$Zn_{0.45}$-$Bi_{0.55}$	750	–	157	–	Graphite sheets	[51]
Bi	750–900	–	308.7	–	Amorphous carbon	[51]
$Ni_{27}Bi_{72}Se_1$	1000	64	201.2	100	Highly graphitized	[53]
$Cu_{45}Bi_{47}Se_8$	1000	50.49	323.3	–	–	[53]
$Bi_{68}Ni_{27}Cu_5$	1040	42	216	40	–	[50]
$Bi_{68}Ni_{27}Mn_5$	1040	42	264	20	–	[50]
Fe(3%)/NaKCl	1000	~9	171	>50	Graphite sheets	[54]
$MnCl_2$(67)-KCl(33)	1050	30	161	>30	Highly graphitized	[55]
$MnCl_2$-KCl	1000	–	152	72	Multilayer graphene	[56]
$CuCl_2$/NaCl-KCl	850	–	–	–	0D CB + 2D graphite composite structure	[58]
NaCl	1000	5.5	231	–	The carbon purity is 91.6% and partial graphitization occurs.	[57]
KCl	1000	5.2	236	–	The carbon purity is 65.5% and amorphous carbon is the main component.	[60]
MoS_2/NaBr-KBr	800	2.75	57	<6	Amorphous carbon	[61]
$CrCl_2$(20)-KCl(80)	1000	12.9	198	–	Bulk/amorphous carbon, local graphitization	
$NiCl_2$(20)-KCl(80)	1000	8	–	Stable after reduction	Metal pollution, amorphous carbon	[61]

This control ranges from amorphous carbon to highly crystalline graphite flakes, graphene, and even multidimensional composite carbon materials. Such advancements offer a flexible and promising technological pathway to achieve the dual objectives of "hydrogen production and carbon production".

2.2.4 Carbon separation strategies for MMC

The separation and purification of solid carbon generated during methane pyrolysis pose significant challenges for its industrial application. Residual metal or salt impurities in carbon products can severely impact the economics and feasibility of their subsequent use or sequestration. Recently, molten media, such as molten salts and molten metals, have shown considerable promise as reaction media for carbon separation in methane pyrolysis. Strategies primarily involve single-phase molten salt systems, two-phase metal-salt systems, and subsequent carbon purification methods (Table 3).

In single-phase molten salt systems, alkali metal halides like NaCl, KCl, NaBr and KBr have garnered increasing attention due to their low cost, environmental friendliness, and water solubility. Parkinson et al.[57] systematically compared the effects of various molten salts on carbon purity, finding a strong correlation with the cation radius of the salt and its wettability with carbon. For instance, NaCl, with the smallest nucleation spacing and lowest adhesion energy, achieved a carbon purity of 91.6% after just water washing. Conversely, KBr, due to its high wettability, resulted in a lower carbon purity of 55.8%. Additionally, Kang et al.[55] discovered that the high density of the molten salt system aids in the separation of carbon products. In the $MnCl_2$-KCl mixed molten salt, carbon products can be effectively separated through flotation or sedimentation, achieving a carbon purity of over 93% after water washing, demonstrating excellent separation performance. This system not only promotes the formation of highly graphitized carbon but also enhances the efficient recovery of carbon products.

Biphasic metal-salt systems effectively purify carbon *in situ* by using a molten metal catalyst, such as a Ni-Bi alloy, covered with a layer of molten salts like NaBr or KBr. Rahimi et al.[62] showed that the dynamics of the melt facilitate the rupture of the metal interface (bubble rupture) as carbon-containing bubbles transition from the metal phase to the salt phase. Consequently, metal droplets return to the bulk metal, and carbon particles rise in the salt, depending on the relative densities of the salt and carbon. As illustrated in Figure 7, carbon forms a distinct surface layer in NaBr, whereas in KBr, it disperses within the salt body, reflecting differences in salt wettability. This approach reduces metal contamination from 83% in a single-phase metal reactor to less than 5%, thereby significantly improving the availability of the carbon product.

The subsequent purification of carbon is essential for improving its quality. Rahimi et al.[62] evaluated three methods for carbon purification including water washing, vacuum heating at 100 °C, and acid washing with 1 mol/L HCl, concluding that vacuum treatment can boost carbon purity from 78.3% to 96.0%, while acid washing can achieve 95.4%. Palmer et al.[63] managed to reduce metal impurities to 0.2%–2% using vacuum distillation, magnetic separation, and hydrochloric acid washing in the Ni-Bi system. However, they noted that these processes are expensive and may impact economic feasibility. Moreover, the morphology and structure of carbon significantly impact the choice of separation strategies. Parkinson et al.[57] discovered a negative correlation between carbon purity and the nuclear distance of salts ($R^2 > 0.93$), noting that higher carbon purity is associated with a greater degree of graphitization. Sheil et al.[61] further observed that carbon produced in the $MnCl_2$-KCl system forms a multi-layer graphene structure, which was easier to separate from the molten salt, while in the pure KCl system, the product was amorphous carbon.

3 Applications of carbon materials from CH_4 pyrolysis

Realizing high-value utilization of solid carbon by-products is a key economic driver for commercializing methane pyrolysis. Traditional pyrolytic carbon has been treated as a low-value powder (for example, carbon black), but advances in reactor engineering and process design now enable direct synthesis of advanced carbon materials with controlled morphology and macroscopic structure. Recent progress shows a clear shift from batch powder collection toward continuous or semi-continuous processes capable of producing carbon materials suitable for high-performance applications.

Table 3 Summary of carbon separation strategies

Separation strategy	Reaction medium	Carbon purity (after water washing)	Subsequent purification method	Carbon morphology characteristics	Reference
Single-phase molten salt	NaCl, KCl, NaBr, KBr	55.0%–91.6%	Water washing only	Low density, high porosity, low graphitization	[62]
Single-phase catalytic molten salt	$MnCl_2$-KCl	>93%	Water washing+heat treatment	Highly graphitized, flake-like structure	[61]
Two-phase metal-salt	Ni-Bi + NaBr/KBr	Metal contamination <5%	Water washing + vacuum/acid washing, >95% carbon purity	Carbon black, nanotubes, mixed flakes	[63]
Pure metal system	Ni-Bi alloy	~61%	Vacuum + magnetic separation + acid washing	Amorphous to graphitized mixture	[31]

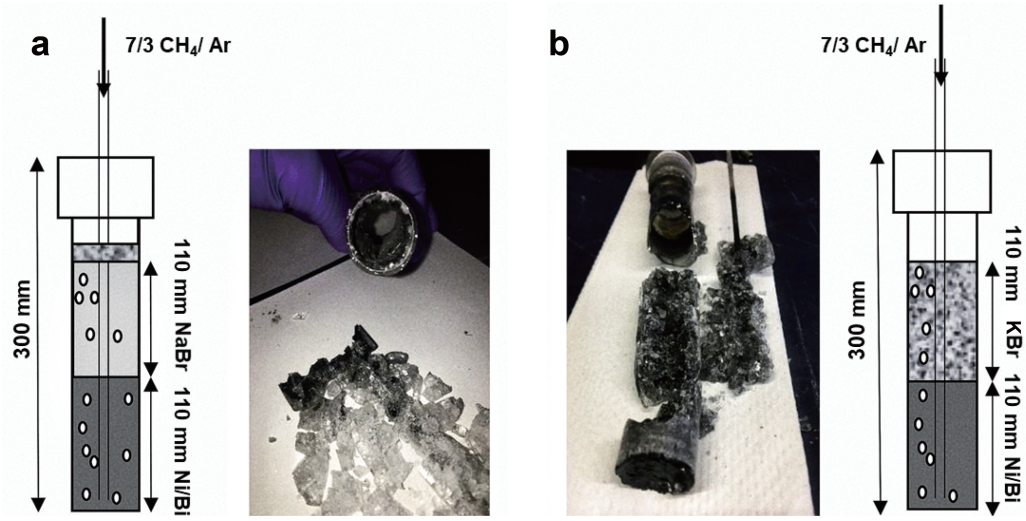


Fig. 7 Photographs of the cooled salt phase containing the carbon produced after conversion of approximately 1.0 g of methane in 42 mL of molten Ni/Bi and 42 mL of salt at 1000 °C: (a) NiBi/NaBr (110∶110); (b) NiBi/KBr (110∶110)[62] (with permission from Elsevier)

Reactor innovation is the principal driver of this transformation. For example, Sun et al.[64] developed a semi-continuous fluidized-bed process that operates at 850 °C using a Fe/θ-Al_2O_3 catalyst (Figure 8(a)). The process couples methane pyrolysis with steam-assisted fluidization to exfoliate CNTs *in situ* in a cyclic mode, producing a cumulative hydrogen yield of 1059 mmol/g over 10 cycles. The resulting CNTs can be processed into free-standing CNT films. These films combine high electrical conductivity and optical transparency, providing a practical route from methane-derived CNTs to macroscopic materials for flexible electronics and transparent electrodes. Peden et al.[64] demonstrated a more integrated and advanced approach. They designed a multi-channel floating catalyst chemical vapor deposition reactor in which the recycling rate of process gas during operation reached approximately 99% (Figure 8(b))[65].

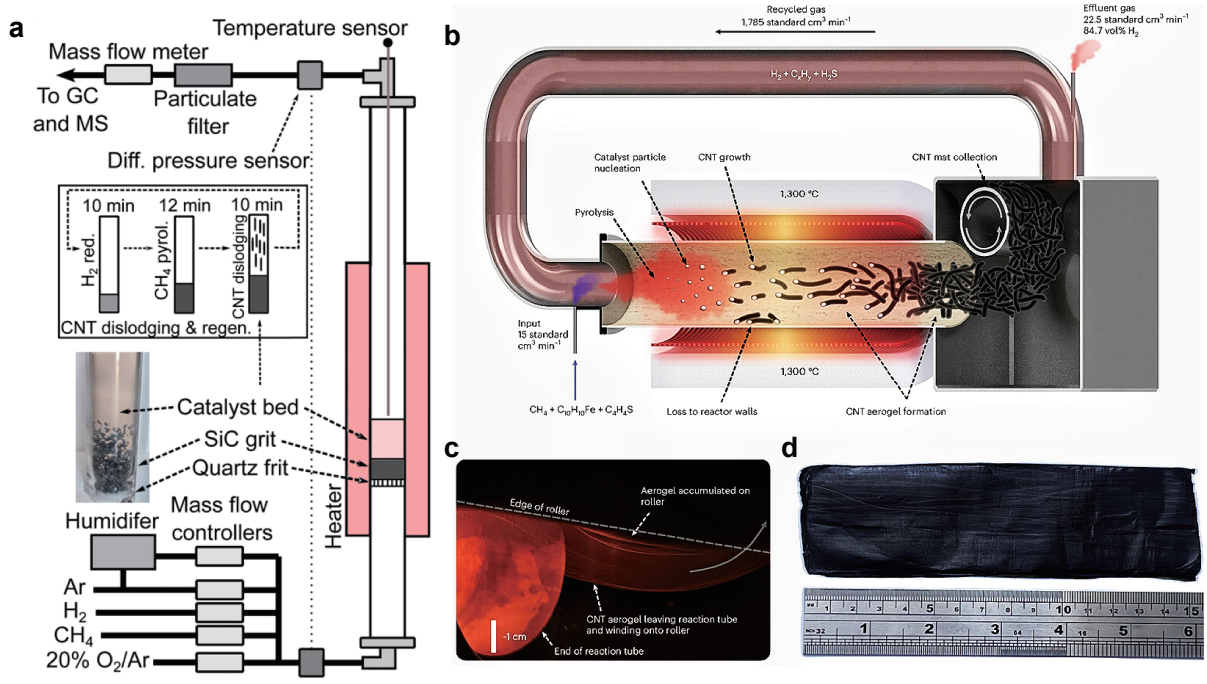


Fig. 8 (a) Schematic diagram of a fluidized bed reactor for methane pyrolysis[64]; (b) Schematic of the multi-pass reactor, showing ~99% recycled process gas, CNT production and hydrogen effluent leaving the reactor[65]; (c) Photograph of the CNT aerogel leaving the reaction tube and winding onto the collection roller[65]; (d) Photograph of a mat made of multiple layers of CNT aerogel after removal from the reactor[65] (with permission from Elsevier, Springer Nature)

This configuration directly converted methane into hydrogen (with a purity of 84.7% in the effluent gas) and CNT aerogel—a continuous, porous macroscopic assembly of CNTs—without any external hydrogen supply. The aerogel could be continuously wound and collected from the reactor and then densified into felts or fibers (Figure 8 (c), (d))[65]. The CNTs obtained exhibited a high degree of graphitization, with a Raman I_G/I_D ratio reaching up to 6, which makes them suitable for high-strength, highly conductive structural composites, battery electrodes, and lightweight conductive textiles. This case highlights how reactor and process design can directly couple hydrogen production with the synthesis of advanced carbon structural materials that have high market value.

Beyond carbon nanotubes, carbon materials derived from methane pyrolysis also show strong potential for high-performance applications after refinement or direct use. In electrochemical energy storage, Pan et al.[66] demonstrated that graphitic carbon produced by methane pyrolysis with iron ore as a catalyst—after high-temperature or electrochemical purification (purities of 99.32% and 97.59%, respectively)—functions as an effective electrode material for dual-carbon batteries. The assembled cells exceed those using commercial graphite in energy density, rate capability, and cycling stability. Solid by-products of methane pyrolysis can also be valuable. Yao et al.[67] reported that iron-encapsulated carbon nanoparticles (Fe@C) formed during pyrolysis act as efficient, recyclable heterogeneous Fenton catalysts for degrading various organic pollutants; their magnetic recoverability substantially reduces iron sludge generation and lowers water-treatment cost. In addition, this graphitic carbon serves as an excellent conductive additive. Pan et al.[68] further showed that purified graphitic carbon from methane pyrolysis creates a more effective conductive network in zinc-carbon batteries, delivering superior rate performance and long-term stability compared with commercial carbon black additives.

In summary, innovations in reactor and process design are the principal drivers of methane cracking technology transformation and upgrading. These advances have shifted the field from a single-process focus—primarily hydrogen production with low-value solid carbon as a by-product—into an efficient dual-output platform. Through coordinated control of catalysts and reactors, the process now yields "turquoise hydrogen" and high-performance carbon materials with tunable structures and defined morphologies. The carbon products include conductive films, high-strength fibers, and porous aerogels, which can be deployed directly in higher-value applications such as energy storage, lightweight composites, flexible electronics, and environmental-catalysis. Channeling carbon outputs to these performance-driven markets not only markedly improves the overall economics of methane cracking but also generates revenue that can substantially offset hydrogen production costs, thus creating an essential pathway to commercialization.

4 Conclusions and outlook

Catalytic methane pyrolysis is an emerging technology that produces CO_2-free hydrogen and solid carbon simultaneously, addressing global energy decarbonization needs. This paper systematically reviews and compares progress in the two principal approaches: solid-catalyst systems and molten-medium catalytic systems.

For solid catalysts, relatively high initial activity can be obtained under medium-temperature conditions, but long-term stability is fundamentally constrained by carbon deposition and reactor blockage. Recent studies show carbon deposition is not only the end point of deactivation but also an active participant in the dynamic evolution at the carbon-catalyst interface. Approaches such as active-site regulation, alloying, support modification, and interface decoration can delay deactivation and partially control carbon morphology. However, continuous removal of carbon is difficult in fixed-bed configurations, which limits prospects for large-scale application. By contrast, molten-medium systems address catalyst deactivation and carbon separation by providing a continuously renewable gas-liquid reaction interface. In molten-metal systems (e.g., Ni-Bi, Sn-Ni), a dynamic liquid-solid interface supports sustained operation and promotes flotation and recovery of graphitized carbon. In catalytic molten-salt systems, Lewis-acidic species markedly lower activation barriers and permit controlled tuning of carbon morphology from amorphous deposits to highly graphitized sheets or multilayer graphene. Reaction-environment design, including bubble dynamics and interfacial properties, strongly influences conversion efficiency and the resulting carbon structure. Robust separation and purification methods now enable recovery of high-purity carbon from the molten medium, increasing the technology's practicality. Furthermore, carbon by-products are treated as value-added materials—conductive films, composite reinforcements, energy-storage components, and functional aerogels—thereby improving process economics.

Looking forward, commercializing methane pyrolysis will require coordinated innovation in catalyst design, reactor engineering, system integration, and enhancement of carbon value. First, reaction-mechanism insights must be integrated with catalyst development to produce systems that achieve high carbon selectivity at lower temperatures. Second, informed by detailed understanding of hydrodynamics, mass transfer, and interfacial behavior, reactor configurations must be designed for scalability, high efficiency, and operational stability. At the same time, the overall techno-economics should be improved through energy-integration optimization, cost control, and process cycle design. Efforts should also promote the transition of carbon coproducts from low-value byproducts to high-value materials, using standardized quality control and broader application development to boost market competitiveness. Only by integrating catalytic science, engineering, and materials applications across these dimensions can methane pyrolysis evolve into a sustainable, competitive "hydrogen-

carbon" coproduction platform that reliably supports a low-carbon energy system and a circular carbon economy.

Declaration of Competing Interest

The authors declare no conflict of interest.

References

[1] MASSON-DELMOTTE V, ZHAI P, PÖRTNER H O, et al. Global warming of 1.5 °C[J]. IPCC Special Report, 2018, 1(5): 43−50.

[2] SHUKLA P R, SKEA J, SLADE R, et al. Climate change 2022: Mitigation of climate change[J]. IPCC AR6 WGIII, 2022, 10: 9781009157926.

[3] STAFFELL I, SCAMMAN D, ABAD A V, et al. The role of hydrogen and fuel cells in the global energy system[J]. Energy Environ Sci, 2019, 12(2): 463−491.

[4] GIELEN D, TAIBI E, MIRANDA R. Hydrogen: A reviewable energy perspective[R]. IRENA, 2019.

[5] HOWARTH R W, JACOBSON M Z. How green is blue hydrogen?[J]. Energy Sci Eng, 2021, 9(10): 1676−1687.

[6] MAC DOWELL N, FENNELL P S, SHAH N, et al. The role of CO_2 capture and utilization in mitigating climate change[J]. Nat Clim Change, 2017, 7(4): 243−249.

[7] MOGHADDAM A L, HEJAZI S, FATTAHI M, et al. Methane pyrolysis for hydrogen production: Navigating the path to a net zero future[J]. Energy Environ Sci, 2025, 18(6): 2747−2790.

[8] BELLOTTI D, RIVAROLO M, MAGISTRI L. A comparative techno-economic and sensitivity analysis of Power-to-X processes from different energy sources[J]. Energy Convers Manage, 2022, 260: 115565.

[9] UECKERDT F, BAUER C, DIRNAICHNER A, et al. Potential and risks of hydrogen-based e-fuels in climate change mitigation[J]. Nat Clim Change, 2021, 11(5): 384−393.

[10] SCHNEIDER S, BAJOHR S, GRAF F, et al. State of the art of hydrogen production via pyrolysis of natural gas[J]. ChemBioEng Rev, 2020, 7(5): 150−158.

[11] SONG J, PARK S. Review of methane pyrolysis for clean turquoise hydrogen production[J]. J Anal Appl Pyrolysis, 2024, 183: 106727.

[12] ZHAO P, POH C K, GAO J, et al. CH_4 decomposition over carbon for CO_2-free hydrogen production: A combined DFT and experimental investigation on the role of carbon[J]. ACS Catal, 2025, 15(18): 16333−16343.

[13] WANG H Y, LUA A C. Hydrogen production by thermocatalytic methane decomposition[J]. Heat Transfer Eng, 2013, 34(11/12): 896−903.

[14] ASHIK U P M, DAUD W M A W, ABBAS H F. Production of greenhouse gas free hydrogen by thermocatalytic decomposition of methane—A review[J]. Renewable Sustainable Energy Rev, 2015, 44: 221−256.

[15] IIDA T. Physical properties of liquid metals surface tension and electronic transport properties of liquid metals[J]. Weld Int, 1994, 8(10): 766−770.

[16] CHEN L, SONG Z, ZHANG S, et al. Ternary NiMo-Bi liquid alloy catalyst for efficient hydrogen production from methane pyrolysis[J]. Science, 2023, 381(6660): 857−861.

[17] SALIPIRA K, COVILLE N J, SCURRELL M S. Carbon produced by the catalytic decomposition of methane on nickel: Carbon yields and carbon structure as a function of catalyst properties[J]. J Nat Gas Sci Eng, 2016, 32: 501−511.

[18] YANG L, WU X, LIU F, et al. Joint-use of activated carbon and carbon black to enhance catalytic stability during chemical looping methane decomposition process[J]. Int J Hydrogen Energy, 2020, 45(24): 13245−13255.

[19] TZENG S S, HUNG K H, KO T H. Growth of carbon nanofibers on activated carbon fiber fabrics[J]. Carbon, 2006, 44(5): 859−865.

[20] SHILAPURAM V, OZALP N, OSCHATZ M, et al. Hydrogen production from catalytic decomposition of methane over ordered mesoporous carbons (CMK-3) and carbide-derived carbon (DUT-19)[J]. Carbon, 2014, 67: 377−389.

[21] MURADOV N, SMITH F, ALI T. Catalytic activity of carbons for methane decomposition reaction[J]. Catal Today, 2005, 102: 225−233.

[22] MURADOV N. Catalysis of methane decomposition over elemental carbon[J]. Catal Commun, 2001, 2(3/4): 89−94.

[23] URDIANA G, VALDEZ R, LASTRA G, et al. Production of hydrogen and carbon nanomaterials using transition metal catalysts through methane decomposition[J]. Mater Lett, 2018, 217: 9−12.

[24] PUDUKUDY M, YAKOB Z, JIA Q, et al. Catalytic decomposition of methane over rare earth metal (Ce and La) oxides supported iron catalysts[J]. Appl Surf Sci, 2019, 467: 236−248.

[25] QIAN J X, CHEN T W, ENAKONDA L R, et al. Methane decomposition to produce CO_x-free hydrogen and nano-carbon over metal catalysts: A review[J]. Int J Hydrogen Energy, 2020, 45(15): 7981−8001.

[26] CUNHA A F, ÓRFÃO J J M, FIGUEIREDO J L. Methane decomposition on Ni–Cu alloyed Raney-type catalysts[J]. Int J Hydrogen Energy, 2009, 34(11): 4763−4772.

[27] LUA A C, WANG H Y. Hydrogen production by catalytic decomposition of methane over Ni-Cu-Co alloy particles[J]. Appl Catal B: Environ, 2014, 156: 84−93.

[28] WANG G, JIN Y, LIU G, et al. Production of hydrogen and nanocarbon from catalytic decomposition of methane over a Ni–Fe/Al_2O_3 catalyst[J]. Energy Fuels, 2013, 27(8): 4448−4456.

[29] LIM K H, CAO K, LI C, et al. Strong metal-support interactions in Ni/KCC-1 catalysts for base-growth carbon nanotubes in methane decomposition[J]. ACS Catal, 2025, 15: 16221−16235.

[30] XUE Q, QIAN S, LIM K H, et al. Nanoscale core–shell catalysts for H_2 production by methane decomposition: Supported nickel nanoparticles ensheathed in metal oxides[J]. J Am Chem Soc, 2025, 147(42): 38141−38157.

[31] ATASHI N, PALOMARES A, VERZIAGGI N, et al. Carbon-induced metal growth and size-dependent activity in methane splitting on nickel nanoparticle catalysts for CO_x-free hydrogen production[J]. Appl Catal B: Environ, 2025,

366: 125817.

[32] PUDUKUDY M, YAKOB Z, MAZUKI M Z, et al. One-pot sol-gel synthesis of MgO nanoparticles supported nickel and iron catalysts for undiluted methane decomposition into CO_x free hydrogen and nanocarbon[J]. Appl Catal B: Environ, 2017, 218: 298−316.

[33] YANG S Y, YUN J S, PARK H W, et al. Unveiling the role of metal–support interactions in Ni catalysts for CO_2 free hydrogen and carbon nanotube production via methane pyrolysis[J]. Int J Hydrogen Energy, 2025, 152: 150168.

[34] KUTTERI D A, WANG I W, SAMANTA A, et al. Methane decomposition to tip and base grown carbon nanotubes and CO_x-free H_2 over mono- and bimetallic 3d transition metal catalysts[J]. Catal Sci Technol, 2018, 8(3): 858−869.

[35] SIKANDER U, SAMSUDIN M F, SUFIAN S, et al. Tailored hydrotalcite-based Mg-Ni-Al catalyst for hydrogen production via methane decomposition: Effect of nickel concentration and spinel-like structures[J]. Int J Hydrogen Energy, 2019, 44(28): 14424−14433.

[36] CALGARO C O, PEREZ-LOPEZ O W. Decomposition of methane over $Co_{3-x}Al_xO_4$ (x=0–2) coprecipitated catalysts: The role of Co phases in the activity and stability[J]. Int J Hydrogen Energy, 2017, 42(50): 29756−29772.

[37] XI W, WANG K, SHEN Y, et al. Dynamic co-catalysis of Au single atoms and nano-porous Au for methane pyrolysis[J]. Nat Commun, 2020, 11(1): 1919.

[38] INGALE G U, PARK D H, YANG C W, et al. Low-carbon hydrogen production by molten metal–catalyzed methane pyrolysis: catalysts, reactor design, and process development[J]. Renewable Sustainable Energy Rev, 2025, 208: 114999.

[39] MEHRABIAN N, SEYFAEE A, NATHAN G J, et al. A numerical investigation of methane pyrolysis in a molten catalyst Bath—A single bubble approach[J]. Int J Hydrogen Energy, 2023, 48(52): 19917−19935.

[40] SUN Z, PARKINSON B, AGBEDE O O, et al. Noninvasive differential pressure technique for bubble characterization in high-temperature opaque systems[J]. Ind Eng Chem Res, 2020, 59(13): 6236−6246.

[41] IGUCHI M, KAWABATA H, NAKAJIMA K, et al. Measurement of bubble characteristics in a molten iron bath at 1600 °C using an electroresistivity probe[J]. Metall Mater Trans B, 1995, 26(1): 67−74.

[42] MORI K, SANO M, SATO T. Size of bubbles formed at single nozzle immersed in molten iron[J]. Trans Iron Steel Inst Jpn, 1979, 19(9): 553−558.

[43] OKAJIMA R, MITCHELL T R, LEONARDI C R, et al. Hydrodynamics of molten media bubble columns for hydrogen production through methane pyrolysis[J]. Phys Fluids, 2024, 36: 103347.

[44] WANG K, LI W S, ZHOU X P. Hydrogen generation by direct decomposition of hydrocarbons over molten magnesium[J]. J Mol Catal A: Chem, 2008, 283(1/2): 153−157.

[45] GEIßLER T, ABÁNADES A, HEINZEL A, et al. Hydrogen production via methane pyrolysis in a liquid metal bubble column reactor with a packed bed[J]. Chem Eng J, 2016, 299: 192−200.

[46] PÉREZ B J L, JIMÉNEZ J A M, BHARDWAJ R, et al. Methane pyrolysis in a molten gallium bubble column reactor for sustainable hydrogen production: Proof of concept & techno-economic assessment[J]. Int J Hydrogen Energy, 2021, 46(7): 4917−4935.

[47] UPHAM D C, AGARWAL V, KHECHFE A, et al. Catalytic molten metals for the direct conversion of methane to hydrogen and separable carbon[J]. Science, 2017, 358(6365): 917−921.

[48] ZENG J, TARAZKAR M, PENNEBAKER T, et al. Catalytic methane pyrolysis with liquid and vapor phase tellurium[J]. ACS Catal, 2020, 10(15): 8223−8230.

[49] DAYAH M. Ptable periodic table[EB/OL]. 2024[2025-11-20]. https://ptable.com/#Properties/Series.

[50] HAN S J, SEO J C, PARK G, et al. Novel descriptor-driven design of molten alloys for methane pyrolysis[J]. ACS Catal, 2024, 14(19): 14787−14795.

[51] KIM T, LEE J, KO Y, et al. Catalytic molten Zn-Bi alloys for methane pyrolysis[J]. Chem Eng J, 2025, 509: 161304.

[52] SCHEIBLEHNER D, NEUSCHITZER D, WIBNER S, et al. Hydrogen production by methane pyrolysis in molten binary copper alloys[J]. Int J Hydrogen Energy, 2023, 48(16): 6233−6243.

[53] SON J H, PARK G, LEE D H, et al. Selenium-promoted molten metal catalysts for methane pyrolysis: Modulating surface tension and catalytic activity[J]. Appl Catal B: Environ, 2025, 366: 125009.

[54] KANG D, PALMER C, MANNINI D, et al. Catalytic methane pyrolysis in molten alkali chloride salts containing iron[J]. ACS Catal, 2020, 10(13): 7032−7042.

[55] KANG D, RAHIMI N, GORDON M J, et al. Catalytic methane pyrolysis in molten $MnCl_2$-KCl[J]. Appl Catal B: Environ, 2019, 254: 659−666.

[56] BAE D, KIM Y, KO E H, et al. Methane pyrolysis and carbon formation mechanisms in molten manganese chloride mixtures[J]. Appl Energy, 2023, 336: 120810.

[57] PARKINSON B, PATZSCHKE C F, NIKOLIS D, et al. Methane pyrolysis in monovalent alkali halide salts: Kinetics and pyrolytic carbon properties[J]. Int J Hydrogen Energy, 2021, 46(9): 6225−6238.

[58] ZHAO Y, SHI Z, ZHU Y, et al. Mechanism for one-pot synthesis of 0D-2D carbon materials in the bubbles inside molten salts[J]. Adv Funct Mater, 2022, 32(42): 2202381.

[59] SCHEIBLEHNER D, NEUSCHITZER D, WIBNER S, et al. The catalytic effect of Ni in methane pyrolysis using molten SnNi alloys for hydrogen production[J]. Int J Hydrogen Energy, 2025, 102: 1045−1054.

[60] MCCONNACHIE M, SHEIL A, KONAROVA M, et al. Evaluation of heterogeneous metal-sulfide molten salt slurry systems for hydrogen production through methane pyrolysis[J]. Int J Hydrogen Energy, 2024, 49: 981−991.

[61] SHEIL A, KONAROVA M, SMART S. Catalytic alkali and transition metal cations to produce low-emission hydrogen from methane pyrolysis[J]. ACS Sustainable Chem Eng, 2023, 11(30): 11248−11258.

[62] RAHIMI N, KANG D, GELINAS J, et al. Solid carbon production and recovery from high temperature methane pyrolysis in bubble columns containing molten metals and

molten salts[J]. Carbon, 2019, 151: 181−191.
[63] PALMER C, BUNYAN E, GELINAS J, et al. CO_2-free hydrogen production by catalytic pyrolysis of hydrocarbon feedstocks in molten Ni–Bi[J]. Energy Fuels, 2020, 34(12): 16073−16080.
[64] SUN E, ZHAI S, KIM D, et al. A semi-continuous process for co-production of CO_2-free hydrogen and carbon nanotubes via methane pyrolysis[J]. Cell Rep Phys Sci, 2023, 4(4): 101338.
[65] PEDEN J, RYLEY J, TERRONES J, et al. Production of hydrogen and carbon nanotubes from methane using a multi-pass floating catalyst chemical vapour deposition reactor with process gas recycling[J]. Nat Energy, 2026, 11(1): 121−134.
[66] PAN Y, CAO L, YAO Y, et al. Graphitic Co-Products of clean hydrogen production enabling high-rate-performance dual-carbon batteries[J]. Adv Energy Mater, 2023, 13(22): 2300495.
[67] YAO Y, LAI L, YU Z, et al. Carbon/iron by-product from catalytic methane decomposition as recyclable Fenton catalyst for pollutant degradation[J]. J Hazard Mater, 2022, 437: 129328.
[68] PAN Y, LO V, CAO L, et al. Graphitic carbon from catalytic methane decomposition as efficient conductive additives for zinc-carbon batteries[J]. Carbon, 2022, 192: 84−92.

甲烷热解制氢和碳材料的研究进展

周璐媛[1]，王　阳[1,*]，孙　玉[1]，霍凯旋[1]，董　培[2,*]，吴明铂[1,3,*]

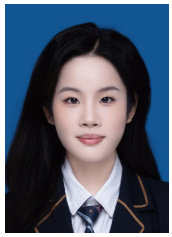
（1. 中国石油大学 (华东) 化学化工学院, 石大山能新能源学院 山东 青岛 266580;
2. 青岛理工大学 环境与市政工程学院, 山东 青岛 266033; 3. 青岛科技大学 化学工程学院, 山东 青岛 266042）

摘　要：社会发展和人类活动加剧了全球变暖和气候变化，亟需发展高效清洁的替代能源以降低碳排放。氢能因其高燃烧值（120 MJ/kg）和净零碳排放的特性，被视为降低碳排放的重要能源载体。近年来，甲烷催化热解制氢备受关注，因为该方法可同时制取高纯度氢气和功能性碳材料。然而，该技术面临的主要挑战包括开发兼具高活性与抗积炭失活的催化剂，以及实现碳产物的高效分离和高值化利用。精确控制活性位点、采用合金化策略、优化载体以及调控碳-催化剂界面可显著提高固体催化剂的抗积炭性能。而引入熔融介质催化体系，利用其动态更新的气-液反应界面，则能从本质上缓解催化剂失活问题，并实现碳产物的连续分离。本工作综述了用于甲烷热解制氢和制碳过程中的固体和熔融介质催化剂的研究进展，重点阐述了其反应机理、催化性能及碳形态调控机制，也对熔融介质中碳产物的分离提纯策略进行了探讨，并对碳材料的高值化应用前景进行了展望。

关键词：甲烷热解；制氢；碳材料；熔融介质

中图分类号：TQ426.94　　**文献标识码：**A

作者简介：



周璐媛（2002），硕士研究生，研究方向为甲烷的高效资源化利用，主要致力于甲烷干重整与甲烷裂解制氢两个方向，by2103010626@s.upc.edu.cn。



董培（1990），博士，副教授，主要研究方向包括纳米功能材料设计及环境污染修复应用、电化学工业废水处理与资源化、碳基催化材料开发及能源催化领域应用，dongpei@upc.edu.cn。



王阳（1991），博士，教授，研究方向为能源与碳一催化研究，包括碳基催化材料设计开发及其能源催化转化应用，CO_2 和 CO 等碳一小分子转化制乙醇、芳烃等宏/微观跨尺度催化体系构建，wangyang@upc.edu.cn。



吴明铂（1972），博士，教授，主要从事重质油高附加值利用、新型碳材料研发、二氧化碳转化利用等方面工作，wumb@upc.edu.cn。